The Astrophysical Journal, 865:98 (14pp), 2018 October 1 https://doi.org/10.3847/1538-4357/aadcee

Oxygen Isotopic Exchange between Amorphous Silicate and Water Vapor and Its Implications for Oxygen Isotopic Evolution in the Early Solar System

Daiki Yamamoto[1], Minami Kuroda[1], Shogo Tachibana[1,2], Naoya Sakamoto[3], and Hisayoshi Yurimoto[1,4]
[1] Department of Natural History Sciences, Hokkaido University, Sapporo, Hokkaido 060-0810, Japan; daiki@ep.sci.hokudai.ac.jp
[2] UTokyo Organization for Planetary Space Science, The University of Tokyo, Hongo, Tokyo 113-0033, Japan
[3] Isotopic Imaging Laboratory, Hokkaido University, Sapporo, 001-0021, Japan
[4] Institute of Space and Astronautical Science, Japan Aerospace Exploration Agency, Sagamihara, Kanagawa, 252-210, Japan
Received 2018 June 28; revised 2018 August 20; accepted 2018 August 22; published 2018 September 26

Abstract

Meteoritic evidence suggests that oxygen isotopic exchange between ^{16}O-rich amorphous silicate dust and ^{16}O-poor water vapor occurred in the early solar system. In this study, we experimentally investigated the kinetics of oxygen isotopic exchange between submicron-sized amorphous forsterite grains and water vapor at protoplanetary disk-like low pressures of water vapor. The isotopic exchange reaction rate is controlled either by diffusive isotopic exchange in the amorphous structure or by the supply of water molecules from the vapor phase. The diffusive oxygen isotopic exchange occurred with a rate constant D ($m^2\,s^{-1}$) $= (1.5 \pm 1.0) \times 10^{-19}$ $\exp[-(161.5 \pm 14.1\ (kJ\,mol^{-1}))R^{-1}(1/T - 1/1200)]$ at temperatures below ~800–900 K, and the supply of water molecules from the vapor phase could determine the rate of oxygen isotopic exchange at higher temperatures in the protosolar disk. On the other hand, the oxygen isotopic exchange rate dramatically decreases if the crystallization of amorphous forsterite precedes the oxygen isotopic exchange reaction with amorphous forsterite. According to the kinetics for oxygen isotopic exchange in protoplanetary disks, original isotopic compositions of amorphous forsterite dust could be preserved only if the dust was kept at temperatures below 500–600 K in the early solar system. The ^{16}O-poor signatures for the most pristine silicate dust observed in cometary materials implies that the cometary silicate dust experienced oxygen isotopic exchange with ^{16}O-poor water vapor through thermal annealing at temperatures higher than 500–600 K prior to their accretion into comets in the solar system.

Key words: astrochemistry – meteorites, meteors, meteoroids – methods: laboratory: solid state – protoplanetary disks – stars: protostars

1. Introduction

Oxygen is the third most abundant element in the solar system and could be present in the forms of silicate and oxide dust, ice, and gas (H_2O and CO) in the early solar system. The evolution of these components prior to planet formation has been recorded as variations of oxygen isotopic compositions (^{16}O, ^{17}O, and ^{18}O) in pristine protoplanetary disk materials.

The analysis of solar wind particles returned by the *Genesis* spacecraft discovered that the oxygen isotopic composition of the Sun is enriched in ^{16}O compared to Earth and most extraterrestrial materials but similar to those of refractory inclusions (the oldest solid objects in the solar system) in chondrites (McKeegan et al. 2011). The oxygen isotopic compositions of other extraterrestrial materials and the Earth cannot be explained by mass-dependent isotopic fractionation associated with chemical and/or physical processes from the solar oxygen isotopic composition and require isotopic exchanges with ^{16}O-poor reservoirs in the early solar system.

The ^{16}O-poor reservoir may have been formed as H_2O through self-shielding of carbon monoxide (CO) during isotopically selective photodissociation in the protosolar molecular cloud (Yurimoto & Kuramoto 2004): CO molecules with minor oxygen isotopes ($C^{17}O$ and $C^{18}O$) are dissociated by UV photolysis in the deep interior of the molecular cloud, while the most abundant $C^{16}O$ is not due to self-shielding. This results in enrichment of atomic ^{17}O and ^{18}O in the interior of the molecular cloud, which turns into H_2O molecules through hydrogenation. Such ^{16}O-poor water vapor in the early solar system may be inherited by cosmic symplectite (intergrown iron sulfide and oxide assemblage) with ^{17}O- and ^{18}O-rich isotopic compositions in the Acfer 094 ungrouped carbonaceous chondrite (Sakamoto et al. 2007; Seto et al. 2008; Abe et al. 2017) and the comet 81P/Wild 2 (Nguyen et al. 2017). The cosmic symplectites are considered to have formed through oxidation and sulfidation of Fe–Ni metal with H_2O and H_2S (Sakamoto et al. 2007; Seto et al. 2008).

The oxygen isotopic exchange between pristine dust components with the Sun-like ^{16}O-rich isotopic compositions and ^{16}O-poor water vapor is thus a key process for the oxygen isotopic evolution of solid components in the early solar system. The dominant solid component in the early evolution stage of the protoplanetary disk would be amorphous silicate dust because silicate dust in the interstellar medium is dominantly in the amorphous form (Kemper et al. 2004). The observation of more crystalline silicate dust in the inner part of protoplanetary disks than in the outer part (van Boekel et al. 2005; Ratzka et al. 2007) suggests that thermal annealing of pristine amorphous silicate dust occurs in protoplanetary disks. Therefore, the oxygen isotopic exchange between pristine amorphous silicate dust and water vapor would occur during the thermal annealing in the early solar system and contribute to the oxygen isotopic evolution of early solar system materials. We also note that this isotopic exchange process in the early solar system could have played a role in diminishing and/or erasing the large oxygen isotopic

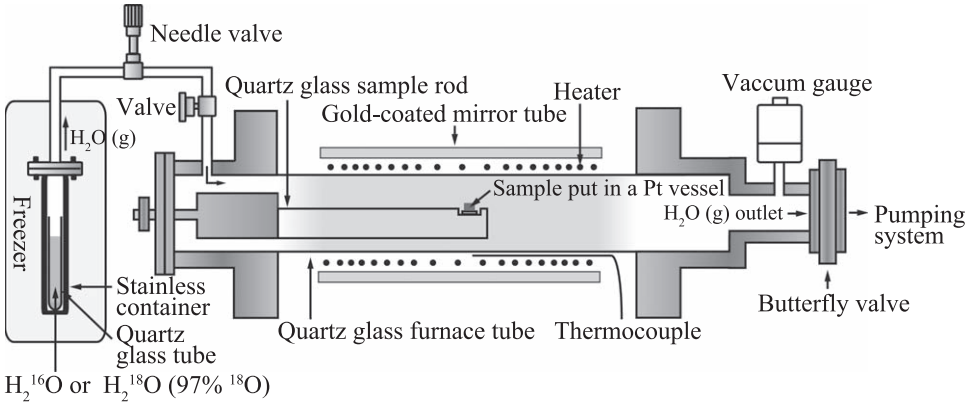

Figure 1. Schematic illustration of the vacuum furnace configuration.

anomalies of presolar silicate grains, which are the original ingredient of the solar system. The abundances of presolar silicate grains in the least-altered chondrites, micrometeorites, and anhydrous interplanetary dust particles range from ~100 to ~500 ppm (Floss & Haenecour 2016), and their low abundances indicate that the thermal destruction of presolar silicate grains occurred in the early solar system prior to accumulation of small planetesimals (Floss & Stadermann 2012; Floss & Haenecour 2016).

Thermal annealing of amorphous silicate dust in protoplanetary disks is important to understand the early chemical evolution of disks and the solar system, but little has been known about the oxygen isotopic exchange reaction between amorphous silicates and water vapor under disk-like low-pressure conditions. This study focuses on the kinetics of oxygen isotope exchange between amorphous forsterite and water vapor, and we performed the isotopic exchange experiments under disk-like low-pressure conditions. We describe the experimental method and the sample analysis in Section 2. The results and discussion of the kinetics of isotopic exchange are described in Sections 3 and 4. We apply the kinetics of the oxygen isotopic evolution of silicate dust in protoplanetary disks in Section 5 and summarize and conclude in Section 6.

2. Experiments

2.1. Heating Experiments

The oxygen isotope exchange experiments between amorphous forsterite and ^{18}O-enriched water vapor were carried out at 803–1073 K under a disk-like water vapor pressure of P_{H2O} = 0.01 and 0.3 Pa using a gold-mirror vacuum furnace (Thermo-Riko GFA 430VN; Figure 1). The furnace consists of a silica glass tube (36 mm in diameter and 450 mm in length) surrounded by an Inconel alloy coil heater and a gold-coated mirror tube, a pumping system (a turbo-molecular pump and a scroll pump), and gas inlets for $H_2{}^{16}O$ and $H_2{}^{18}O$ vapor. The pressure inside the furnace was measured with a Pirani/cold-cathode gauge (Pfeiffer PKR251) using a proper conversion factor for H_2O.

The furnace temperature was measured and controlled by a type-K thermocouple outside of the silica glass tube. The sample temperature in the furnace was calibrated using the melting points of sodium chloride (800.4°C), potassium bromide (730°C), lithium bromide (547°C), and indium (156.6°C) placed at the same location as the sample inside the furnace. The temperature calibration was made both at P_{H2O} = 500 Pa and in vacuum (10^{-4}–10^{-5} Pa). No significant pressure dependence of temperature calibration between P_{H2O} = 500 Pa and in vacuum was found, and a single interpolated regression line for the temperature correction was applied to heat the samples at the desired temperatures under all P_{H2O} conditions. The uncertainty of the sample temperature was ±5°C.

Submicron-sized amorphous forsterite grains were used as a starting material for the experiments. The grains were synthesized by an induced thermal plasma method and have a spherical shape 10–200 nm in diameter (~80 nm in average diameter; Koike et al. 2010). A part of the amorphous grains was annealed at 1073 K for 24 hr in air to obtain crystalline forsterite without severe sintering (Koike et al. 2010), which was used as a reference of isotopically normal crystalline forsterite. About 30 mg of the starting material was used for each experiment. The powder was put in a platinum vessel and placed in a silica glass sample stand in the furnace.

Liquid reagent of $H_2{}^{18}O$ (97-atom% ^{18}O; Sigma-Aldrich) put in a silica glass container was sealed into a stainless container in a nitrogen-purged glove box to eliminate the contribution of $H_2{}^{16}O$ from the ambient gas. Liquid $H_2{}^{18}O$ in the stainless container was frozen in a freezer, and the stainless container was then connected to the gold-mirror vacuum furnace through a gas flow line. The temperature of $H_2{}^{18}O$ was kept at 253 and 243 K for the experiments at P_{H2O} of 0.3 and 0.01 Pa. The gas species in the furnace were monitored by a quadrupole mass spectrometer (HORIBASTEC QL-SG01-065-1A). The most dominant gas species was $H_2{}^{18}O$, and the detected $H_2{}^{16}O/H_2{}^{18}O$ ratio was consistent with $^{16}O/^{18}O$ of the reagent $H_2{}^{18}O$ (97-atom% ^{18}O).

A flow rate of $H_2{}^{18}O$ vapor was adjusted by a needle valve, and a gas evacuation rate was adjusted by a butterfly valve attached to the pumping system. The balance between both the gas flow and evacuation rates determined the P_{H2O} in the furnace. After P_{H2O} stabilized at the room temperature, the sample was heated up from the room temperature to a desired temperature (803–1123 K) in 20 minutes. Then, the sample was kept at the temperature for a desired duration (0–336 hr) and cooled down to the room temperature in ~20 minutes. The P_{H2O} was stable in most runs but occasionally adjusted during experiments if necessary. We also conducted annealing experiments at P_{H2O} of 0.3 Pa using isotopically normal (i.e., ^{16}O-dominant) water for comparison. The experimental conditions are found in Tables 1 and 2.

Table 1
Experimental Conditions and Results for the Sample Annealed with $H_2{}^{16}O$ and $H_2{}^{18}O$ Vapor of 0.3 and 0.01 Pa at 803–883 K

Temperature (K)	P_{H2O} (Pa)	Duration (hr)	Flow Gas	Peak Position (cm^{-1})[a]	$\Delta\kappa/\kappa_0$ (%)	$f^{18}O$ (IR)[b]	$f^{18}O$ (SIMS)[c]
883	0.3	4	$H_2{}^{18}O$	970.74 ± 0.83	1.05 ± 0.09	/	0.19 ± 0.003
883	0.3	6	$H_2{}^{18}O$	967.49 ± 1.73	1.38 ± 0.18	/	0.30 ± 0.018
883	0.3	8	$H_2{}^{18}O$	963.87 ± 0.61	1.75 ± 0.07	/	/
883	0.3	24	$H_2{}^{18}O$	961.94 ± 0.82	1.94 ± 0.09	/	0.47 ± 0.009
883	0.3	48	$H_2{}^{18}O$	crystallized	/	/	/
883	0.3	72	$H_2{}^{18}O$	crystallized	/	/	/
883	0.01	0	$H_2{}^{18}O$	979.28 ± 1.04	0.18 ± 0.11	0.04 ± 0.025	/
883	0.01	4	$H_2{}^{18}O$	977.13 ± 1.49	0.40 ± 0.16	0.08 ± 0.034	/
883	0.01	4	$H_2{}^{18}O$	977.97 ± 1.28	0.31 ± 0.14	0.07 ± 0.030	/
883	0.01	8	$H_2{}^{18}O$	975.27 ± 1.69	0.58 ± 0.18	0.12 ± 0.039	/
883	0.01	15	$H_2{}^{18}O$	973.03 ± 0.24	0.81 ± 0.05	0.17 ± 0.019	/
883	0.01	24	$H_2{}^{18}O$	971.41 ± 1.37	0.98 ± 0.15	0.21 ± 0.036	/
853	0.3	2	$H_2{}^{18}O$	977.54 ± 0.43	0.35 ± 0.06	0.08 ± 0.014	/
853	0.3	3	$H_2{}^{18}O$	974.17 ± 0.73	0.70 ± 0.09	0.15 ± 0.022	/
853	0.3	4	$H_2{}^{18}O$	973.87 ± 1.14	0.73 ± 0.12	/	0.19 ± 0.003
853	0.3	12	$H_2{}^{18}O$	968.77 ± 1.82	1.25 ± 0.19	0.26 ± 0.050	/
853	0.3	16	$H_2{}^{18}O$	967.42 ± 1.26	1.39 ± 0.13	/	0.32 ± 0.007
853	0.3	24	$H_2{}^{18}O$	965.58 ± 2.03	1.57 ± 0.21	/	0.28 ± 0.005
853	0.3	24	$H_2{}^{16}O$	980.14 ± 1.02	0.09 ± 0.11	/	/
853	0.3	48	$H_2{}^{16}O$	982.31 ± 1.50	−0.13 ± 0.16	/	/
853	0.3	72	$H_2{}^{18}O$	962.50 ± 0.65	1.89 ± 0.08	/	0.49 ± 0.01
853	0.3	120	$H_2{}^{18}O$	960.86 ± 0.48	2.05 ± 0.06	/	/
853	0.3	120	$H_2{}^{18}O$	961.94 ± 0.99	1.94 ± 0.11	/	0.51 ± 0.005
853	0.3	168	$H_2{}^{18}O$	961.22 ± 0.72	2.02 ± 0.08	/	0.70 ± 0.006
853	0.3	235	$H_2{}^{18}O$	crystallized	/	/	/
853	0.01	6	$H_2{}^{18}O$	975.80 ± 0.34	0.53 ± 0.05	0.11 ± 0.015	/
853	0.01	12	$H_2{}^{18}O$	973.15 ± 0.62	0.80 ± 0.08	0.17 ± 0.022	/
853	0.01	24	$H_2{}^{18}O$	970.98 ± 1.52	1.02 ± 0.16	0.22 ± 0.039	/
853	0.01	48	$H_2{}^{18}O$	966.16 ± 1.62	1.51 ± 0.17	0.32 ± 0.046	/
853	0.01	72	$H_2{}^{18}O$	962.43 ± 0.99	1.89 ± 0.11	/	/
853	0.01	96	$H_2{}^{18}O$	963.99 ± 1.28	1.73 ± 0.14	/	/
853	0.01	120	$H_2{}^{18}O$	961.82 ± 0.68	1.96 ± 0.08	/	/
853	0.01	168	$H_2{}^{18}O$	961.46 ± 0.91	1.99 ± 0.10	/	/
803	0.3	12	$H_2{}^{18}O$	974.12 ± 1.78	0.70 ± 0.19	0.15 ± 0.042	/
803	0.3	22	$H_2{}^{18}O$	973.27 ± 0.99	0.79 ± 0.11	/	0.18 ± 0.015
803	0.3	48	$H_2{}^{18}O$	969.90 ± 0.91	1.13 ± 0.10	/	0.23 ± 0.002
803	0.3	120	$H_2{}^{18}O$	968.01 ± 1.94	1.33 ± 0.20	0.28 ± 0.050	/
803	0.3	168	$H_2{}^{18}O$	964.96 ± 0.84	1.64 ± 0.09	/	0.37 ± 0.007
803	0.3	336	$H_2{}^{18}O$	962.31 ± 0	1.91 ± 0.04	/	0.44 ± 0.022
803	0.01	36	$H_2{}^{18}O$	973.20 ± 1.16	0.80 ± 0.13	0.17 ± 0.031	/
803	0.01	72	$H_2{}^{18}O$	970.74 ± 0.62	1.05 ± 0.08	0.22 ± 0.026	/
803	0.01	120	$H_2{}^{18}O$	967.03 ± 1.68	1.43 ± 0.18	0.30 ± 0.046	/
803	0.01	168	$H_2{}^{18}O$	965.20 ± 1.41	1.61 ± 0.15	0.34 ± 0.044	/
803	0.01	240	$H_2{}^{18}O$	964.52 ± 1.00	1.68 ± 0.11	/	/
Amorphous forsterite (starting material)				981.01 ± 0.04	0	/	0.0019 ± 0.0001
						/	0.0020 ± 0.00009
						/	0.0023 ± 0.0002
						/	0.0018 ± 0.0001
						/	0.0020 ± 0.0001

Notes. Errors represent the 1σ standard deviations of the means.
[a] The peak wavenumber of the 10 μm infrared feature of amorphous forsterite.
[b] Oxygen isotopic compositions ($^{18}O/(^{18}O + {}^{16}O)$) of samples obtained from $\Delta\kappa/\kappa_0$.
[c] Oxygen isotopic compositions ($^{18}O/(^{18}O + {}^{16}O)$) of samples measured by SIMS.

2.2. Analytical Procedure

The heated samples were analyzed by a Fourier transform infrared spectrometer (JASCO FT-IR 4200) with a spectral resolution of 2 cm^{-1}. A fraction of the samples was mixed with KBr powder with a mass ratio of 1:500, and the mixture (0.2 g) was pressed into a pellet for the analysis. The infrared light path was purged with dry nitrogen gas during the analysis. Peak positions in the obtained infrared spectrum were determined using the software (Spectral manager version2) attached to the

Table 2
Peak Positions of Forsterite Crystallized at 0.3 Pa of $H_2{}^{16}O$ and $H_2{}^{18}O$ Vapor at 953–1123 K

Temperature (K)	Duration (hr)	Starting Material	Flow Gas	Peak Positions (cm^{-1})							
953	2	Amorphous forsterite	$H_2{}^{18}O$	/	/	910.72[a]	/	610[a]	/	/	/
953	4	Amorphous forsterite	$H_2{}^{18}O$	995.5	961.82	903.49	/	605.06[a]	520.20	/	439.69
953	12	Amorphous forsterite	$H_2{}^{18}O$	988.34	/	894.81	/	599.75	517.31	461.39	439.21
953	24	Amorphous forsterite	$H_2{}^{18}O$	981.11	937.24	889.02	804.17[a]	595.90	513.45	459.94	437.76
953	48	Amorphous forsterite	$H_2{}^{18}O$	977.73	935.31	888.54	803.21[a]	595.41	513.94	460.42	437.28
953	92	Amorphous forsterite	$H_2{}^{18}O$	976.77	933.86	887.58	798.39	592.52	512.97	456.57	438.24
953	120	Amorphous forsterite	$H_2{}^{18}O$	976.29	933.86	887.58	797.90	592.52	509.60	458.49	438.24
953	2	Amorphous forsterite	$H_2{}^{16}O$	/	/	914.58[a]	/	610.36[a]	/	/	/
953	12	Amorphous forsterite	$H_2{}^{16}O$	1004.25	961.82	911.68/906.38[b]	844.19	615.18	527.92	467.65	441.14
953	120	Amorphous forsterite[c]	$H_2{}^{16}O$	1004.73	961.82	908.79/903.01[b]	842.26	616.15	526.95	467.65	441.14
1073	2	Amorphous forsterite	$H_2{}^{18}O$	1004.25	960.38	906.86/903.01[b]	842.26	615.66	525.03	465.73	443.07
1073	2	^{18}O-rich amorphous forsterite[c]	$H_2{}^{18}O$	982.55	941.09	885.17	804.65	597.34	510.56	459.46	438.73
1123	72	Crystalline forsterite	$H_2{}^{18}O$	1004.73	961.82	908.31/903.49[b]	842.74	616.63	528.4	466.21	442.58

Notes.
[a] Peak positions determined with naked eyes because of their weak absorbance.
[b] Split peaks.
[c] Amorphous forsterite preheated at 853 K and 0.3 Pa of $H_2^{18}O$ vapor for 120 hr.

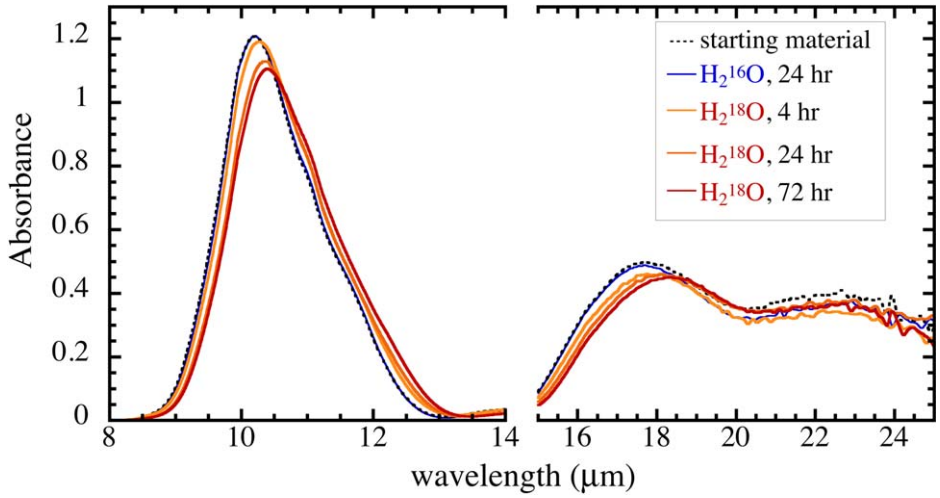

Figure 2. Infrared adsorption spectra of amorphous forsterite used as the starting material (dotted curve) and samples heated at 853 K and 0.3 Pa of $H_2{}^{16}O$ vapor (blue solid curve) or $H_2{}^{18}O$ vapor (orange to red solid curves) for different durations.

spectrometer, and the same sample was measured several times to determine the analytical reproducibility.

The samples were also analyzed with X-ray diffraction (Rigaku SmartLab) for phase determination. The samples were put into a hole (3 mm in diameter and 0.3 mm in depth) on a reflection-free silicon sample holder, and X-ray diffraction patterns were obtained using Cu Kα radiation in the 2θ range from 10° to 70° with a 0.01° step and a scan speed of 1° minute^{-1}.

Oxygen isotope compositions of the samples were measured with secondary ion mass spectrometry (SIMS). In order to obtain a flat surface for SIMS analysis, the powdery samples were shaped into pellets (3 mm in diameter). The pellet, put in a platinum crucible, was sintered in a vacuum furnace (Tachibana et al. 2011) at 10^{-4}–10^{-5} Pa and ~1100°C for more than 1 day. The vacuum furnace was used to prevent the oxygen isotopic exchange with the surrounding atmosphere during sintering. All the pellets turned into crystalline forsterite by annealing, but this does not affect the oxygen isotopic analysis by SIMS. The sintered pellets, mounted into epoxy resin, were polished and gold-coated for the analysis with an ion microprobe (Cameca ims-6f) at Hokkaido University. Depth profiles of ^{16}O and ^{18}O were collected from the surface of pellets using a Cs^+ primary beam 3 nA and 10 kV acceleration voltage with a raster area of 70 μm × 70 μm. Negatively charged secondary ions were collected from the central area of the sputtered region (30 μm in diameter).

Several depth profiles were obtained for each sample until the ion counts of oxygen isotopes became constant, and the oxygen isotopic composition of a sample was determined as an average of the compositions from several different depth profiles. A pellet of forsterite crystallized in the vacuum furnace from the starting material without exposure to $H_2{}^{18}O$ vapor was used as a reference in each analytical session.

3. Results

3.1. Isotopic Exchange at 0.3 Pa of Water Vapor

3.1.1. 803, 853, and 883 K

Most of the samples remained amorphous after annealing except for three samples (883 K for 48 and 72 hr and 853 K for 235 hr) heated for longer durations than others. Typical infrared spectra of amorphous samples heated at 0.3 Pa of $H_2{}^{18}O$ and isotopically normal water vapor ($H_2{}^{16}O$) are compared with the starting material (Figure 2). The starting material has a broad peak attributed to Si–O stretching vibration at ~10.2 μm (981 cm^{-1}). The samples heated at 0.3 Pa of $H_2{}^{16}O$ vapor at 853 K for 24 and 48 hr also show the broad feature with the same peak wavelengths (Figure 2 and Table 1). On the other hand, the peak of amorphous forsterite annealed at 0.3 Pa of $H_2{}^{18}O$ vapor and 803–883 K shifted to a higher wavelength (a lower wavenumber) toward ~10.4 μm (961 cm^{-1}) with heating duration (Figure 2; Table 1). The relative peak shifts of the 10 μm feature ($\Delta\kappa/\kappa_0$), where κ_0 is the peak wavenumber of the starting material and $\Delta\kappa$ represents a difference in peak wavenumbers of the sample and the starting material (κ_0–κ_{sample}), are shown in Figure 3 for the samples heated at 0.3 Pa of $H_2{}^{18}O$ or $H_2{}^{16}O$ vapor (see also Table 1). Although the $\Delta\kappa/\kappa_0$ remains constant within the analytical error for samples heated with $H_2{}^{16}O$ vapor of 0.3 Pa, it increases with time for the samples heated with $H_2{}^{18}O$ vapor for each temperature and becomes almost constant for further heating after it reaches ~2% (Figure 3).

The same trend was observed for the 18 μm absorption feature of amorphous forsterite, representing the Si–O–Si bending vibration, for the samples heated with $H_2{}^{18}O$ vapor (Figure 2).

A linear correlation between $\Delta\kappa/\kappa_0$ for the 10 μm infrared feature and the oxygen isotopic compositions of amorphous forsterite is observed up to $^{18}O/(^{16}O + {}^{18}O)$ ($=f\,{}^{18}O$) of 0.4, where $\Delta\kappa/\kappa_0$ reaches the constant value of ~2% (Figure 4; Table 1). This correlation suggests that $\Delta\kappa/\kappa_0$ for 10 μm infrared features can be used as a scale of oxygen isotopic compositions of amorphous forsterite with $f\,{}^{18}O < \sim 0.4$.

3.1.2. 953 K

Typical infrared spectra of the samples annealed at 953 K and 0.3 Pa of $H_2{}^{18}O$ and $H_2{}^{16}O$ vapor are compared in Figure 5 (see also Table 2 for peak positions of all the samples). The amorphous forsterite gradually crystallizes with time under this temperature, which is also confirmed with X-ray diffraction. Although the spectra of forsterite crystallized in the presence of $H_2{}^{18}O$ vapor resembles overall that of the isotopically normal crystalline forsterite, all the peaks shifted to higher wavelengths (lower wavenumbers) as crystallization proceeded (Figure 5).

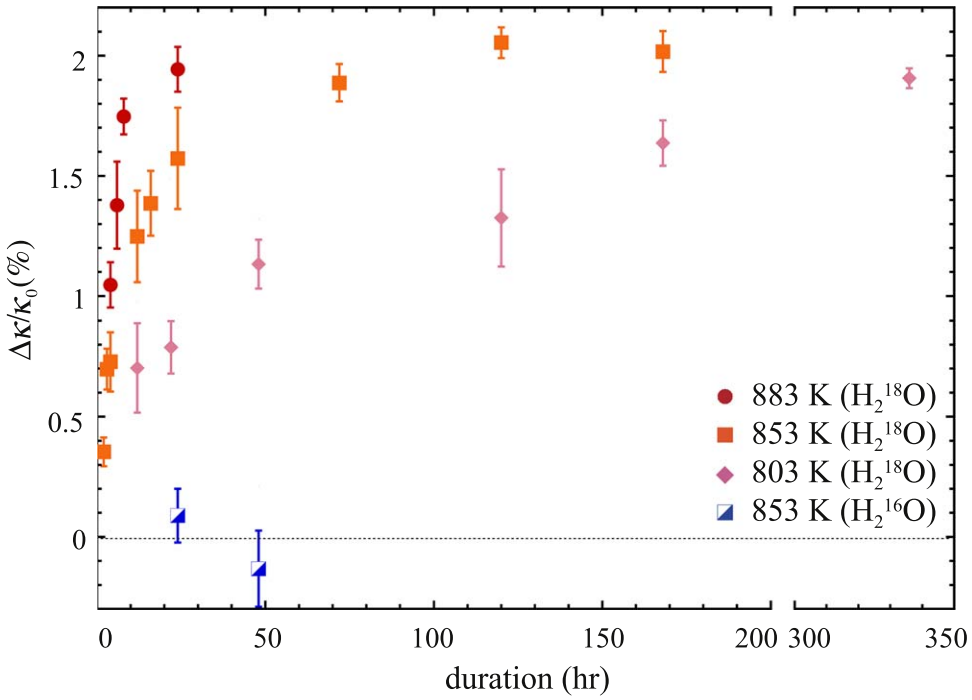

Figure 3. Relative peak shifts ($\Delta\kappa/\kappa_0$; see text in detail) of the 10 μm infrared absorption feature of amorphous forsterite heated at 0.3 Pa of $H_2{}^{18}O$ vapor at 883, 853, and 803 K for different durations. The $\Delta\kappa/\kappa_0$ of the amorphous forsterite heated at 0.3 Pa of $H_2{}^{16}O$ vapor and 853 K are also shown for comparison. Error bars represent the 1σ standard deviations of the means of several measurements of the same sample.

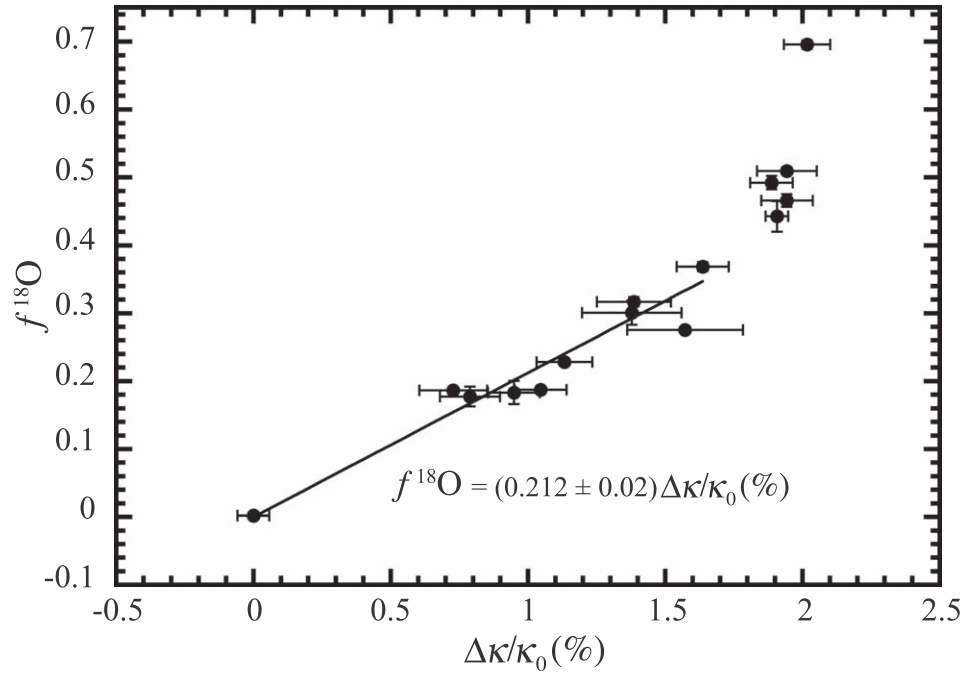

Figure 4. Comparison of the oxygen isotopic composition $f^{18}O = {}^{18}O/({}^{18}O + {}^{16}O)$ and $\Delta\kappa/\kappa_0$. A linear correlation is found between $f^{18}O$ and $\Delta\kappa/\kappa_0$ of $<\sim$1.64%. Error bars are the 1σ standard deviations of the means.

Another notable feature is that the peaks were broader than those of the isotopically normal crystalline forsterite.

3.1.3. 1073 and 1123 K

An infrared spectrum of the sample heated at 1073 K and 0.3 Pa of $H_2{}^{18}O$ vapor for 2 hr matches the crystalline forsterite having the normal oxygen isotopic composition, and neither peak shift nor significant peak broadening was observed (Figure 6; Table 2).

We also conducted a heating experiment at the same condition using the amorphous forsterite that was once annealed at 853 K and 0.3 Pa of $H_2{}^{18}O$ vapor for 120 hr as a starting material. The run product also shows the infrared feature of crystalline forsterite, but all the peaks shifted to longer wavelengths without significant peak broadening (Figure 6; Table 2).

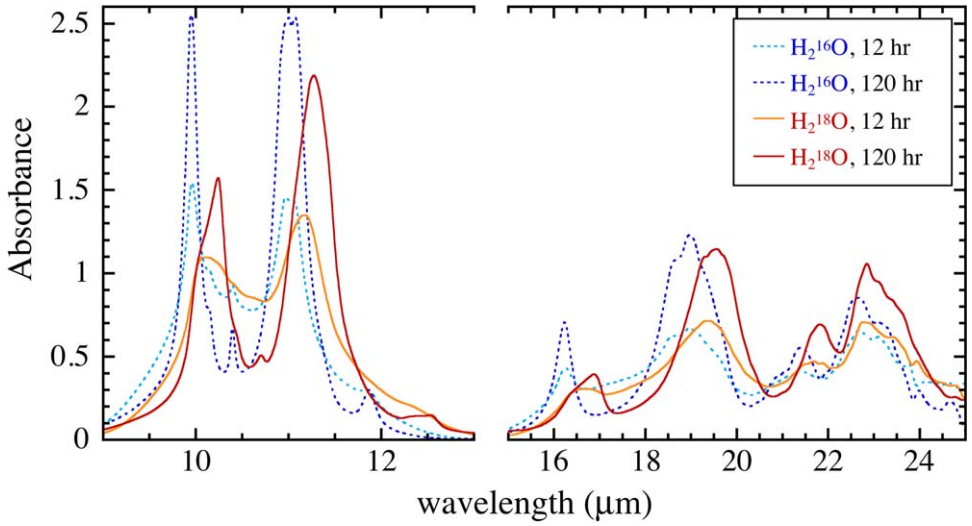

Figure 5. Infrared adsorption spectra of samples heated at 0.3 Pa of $H_2{}^{16}O$ or $H_2{}^{18}O$ vapor for 12 and 120 hr at 953 K.

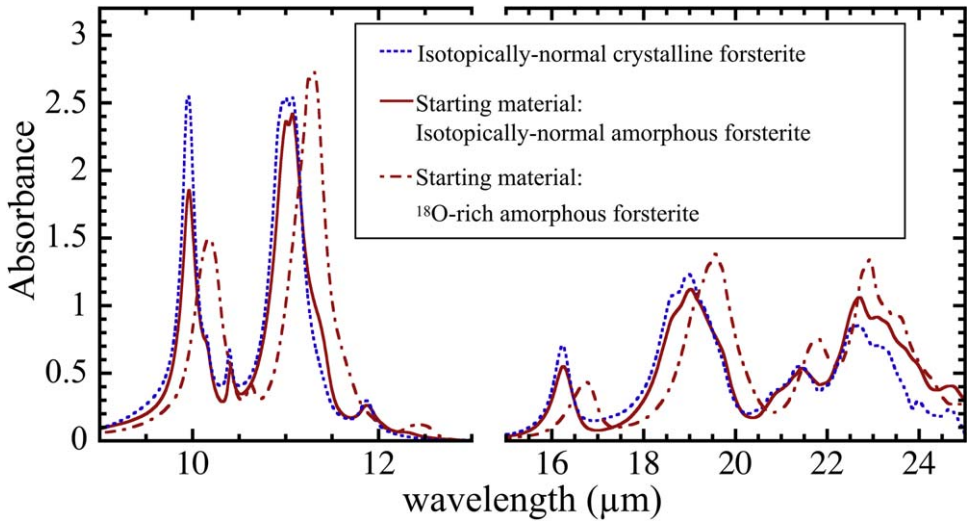

Figure 6. Infrared spectrum of forsterite crystallized at 1073 K and 0.3 Pa of $H_2{}^{18}O$ vapor for 2 hr from the starting material (red solid curve). The spectrum of forsterite crystallized at the same condition from amorphous forsterite that was preheated at 853 K and 0.3 Pa of $H_2{}^{18}O$ vapor for 120 hr is shown as a red dotted-dashed curve. An infrared spectrum of the isotopically normal crystalline forsterite is also shown for comparison (blue dotted curve).

An oxygen isotopic exchange experiment between crystalline forsterite submicron grains and water vapor was also conducted at a higher temperature of 1123 K and 0.3 Pa of $H_2{}^{18}O$ vapor for 72 hr. Neither peak shift nor peak broadening was observed (see also Table 2).

3.2. Isotopic Exchange at 0.01 Pa of Water Vapor

The samples heated at 883, 853, and 803 K and 0.01 Pa of $H_2{}^{18}O$ vapor did not crystallize and remained amorphous. The 10 and 18 μm infrared absorption features shifted to longer wavelengths (shorter wavenumbers) with time as observed in the samples heated at 0.3 Pa of $H_2{}^{18}O$ vapor (Figure 7(a); see also Table 1). The time evolution of $\Delta\kappa/\kappa_0$ of the 10 μm infrared features of the samples heated at 883 and 853 K are similar to each other, suggesting that the oxygen isotopic exchange rates at these temperatures are almost the same.

The time evolution of $\Delta\kappa/\kappa_0$ of the samples heated at 0.01 Pa and 0.3 Pa of $H_2{}^{18}O$ vapor are compared in Figures 7(b)–(d). At 883 K, $\Delta\kappa/\kappa_0$ at 0.01 Pa of $H_2{}^{18}O$ vapor evolves more slowly than that at 0.3 Pa (Figure 7(b)), suggesting that the isotopic exchange rate at 0.01 Pa is smaller than that at 0.3 Pa. The difference between the temporal changes of $\Delta\kappa/\kappa_0$ at 0.01 and 0.3 Pa becomes smaller with decreasing temperature. The isotopic exchange at 0.01 Pa seems to have proceeded with a bit smaller rate than that at 0.3 Pa and 853 K (Figure 7(c)), and it proceeded at a similar rate at 0.01 and 0.3 Pa (Figure 7(d)).

4. Discussion

4.1. Isotopic Exchange Reaction Kinetics at 0.3 Pa of Water Vapor

4.1.1. 803, 853, and 883 K

The oxygen isotopic compositions ($f\ ^{18}O$) of the samples measured with SIMS are normalized to the isotopic composition of $H_2{}^{18}O$ vapor ($f\ ^{18}O = 0.97$) to express the degrees of the isotopic exchange of the sample (α). We also estimated the degrees of the isotopic exchange of the samples that were not measured by SIMS based on the linear correlation between

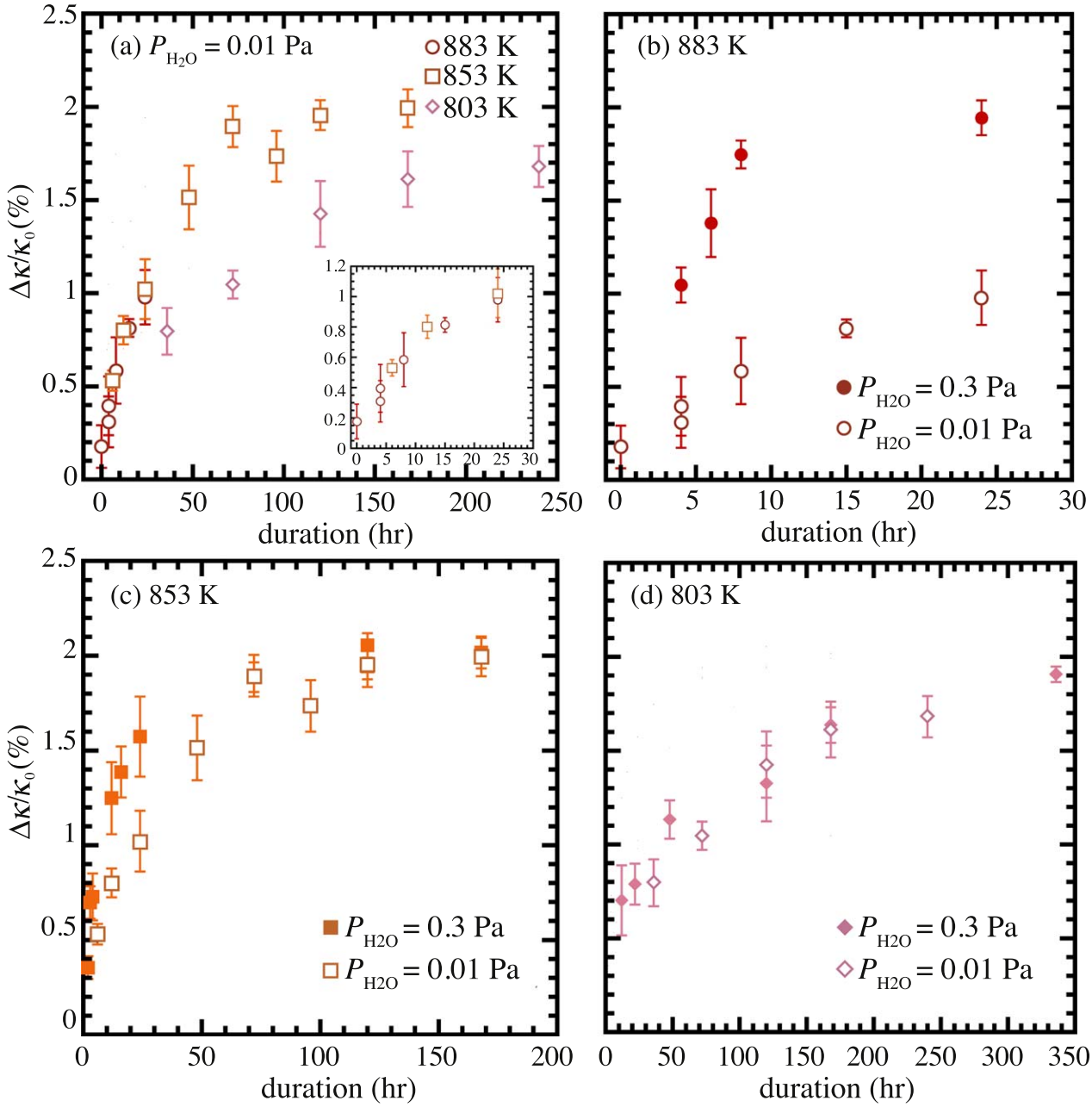

Figure 7. (a) Temporal changes of relative peak shifts ($\Delta\kappa/\kappa_0$) of the 10 μm infrared absorption feature of amorphous forsterite heated at 803, 853, and 883 K and 0.01 Pa of $H_2{}^{18}O$. An inset shows the temporal change of $\Delta\kappa/\kappa_0$ for shorter heating durations. Error bars represent the 1σ standard deviations of the means of several measurements of the same sample. (b) Temporal changes of $\Delta\kappa/\kappa_0$ at 0.01 and 0.3 Pa of $H_2{}^{18}O$ vapor at 883 K. These are also shown at 853 K (panel (c)) and 803 K (panel (d)).

$\Delta\kappa/\kappa_0$ and f ^{18}O (Figure 4) when their $\Delta\kappa/\kappa_0$ values were smaller than 1.64%.

The temporal changes of α of the samples at 0.3 Pa of $H_2{}^{18}O$ vapor do not exhibit linear correlations with heating durations (Figure 8), suggesting that the oxygen isotopic exchange reaction at 0.3 Pa is not controlled by the supply of water molecules. If the supply of water molecules to the grains is the rate-limiting step, α should evolve linearly with time. Another possible process that limits the reaction rate can be the diffusion of water molecules dissolved in the amorphous structure (e.g., Doremus 1969; Kuroda et al. 2018). The temporal change of α for the diffusive exchange reaction in the grains can be given by a three-dimensional diffusion equation in a sphere (Crank 1975),

$$\alpha = 1 - \sum_{n=1}^{\infty} \frac{6}{n^2\pi^2} \exp\left(-\frac{Dn^2\pi^2 t}{r^2}\right), \quad (1)$$

where D is the diffusive isotopic exchange rate constant, r is a grain radius (40 nm on average for the samples in this study), and t is time. The α was reasonably well fitted with Equation (1) (Figure 8), and thus we conclude that the rate-limiting step at 0.3 Pa of water vapor is the diffusive exchange reaction between amorphous forsterite and water molecules. The diffusive isotopic exchange rate constants D at 0.3 Pa of water vapor were calculated to be $(4.9 \pm 0.6) \times 10^{-23}$,

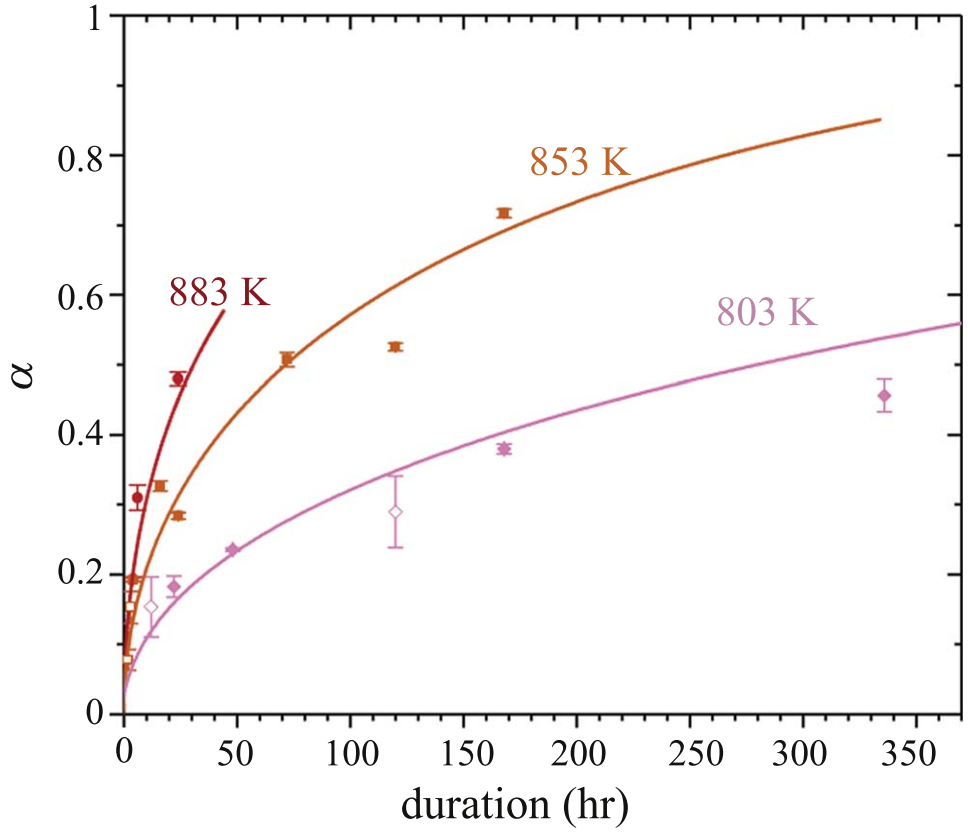

Figure 8. Time evolution of the degree of oxygen isotopic exchange (α) at 0.3 Pa of $H_2{}^{18}O$ vapor and 803, 853, and 883 K. The solid curves represent the fitting results by Equation (1). Filled symbols are the data measured by SIMS, and open symbols are those estimated from $\Delta\kappa/\kappa_0$ (%) of samples. Error bars are the 1σ standard deviations of the means.

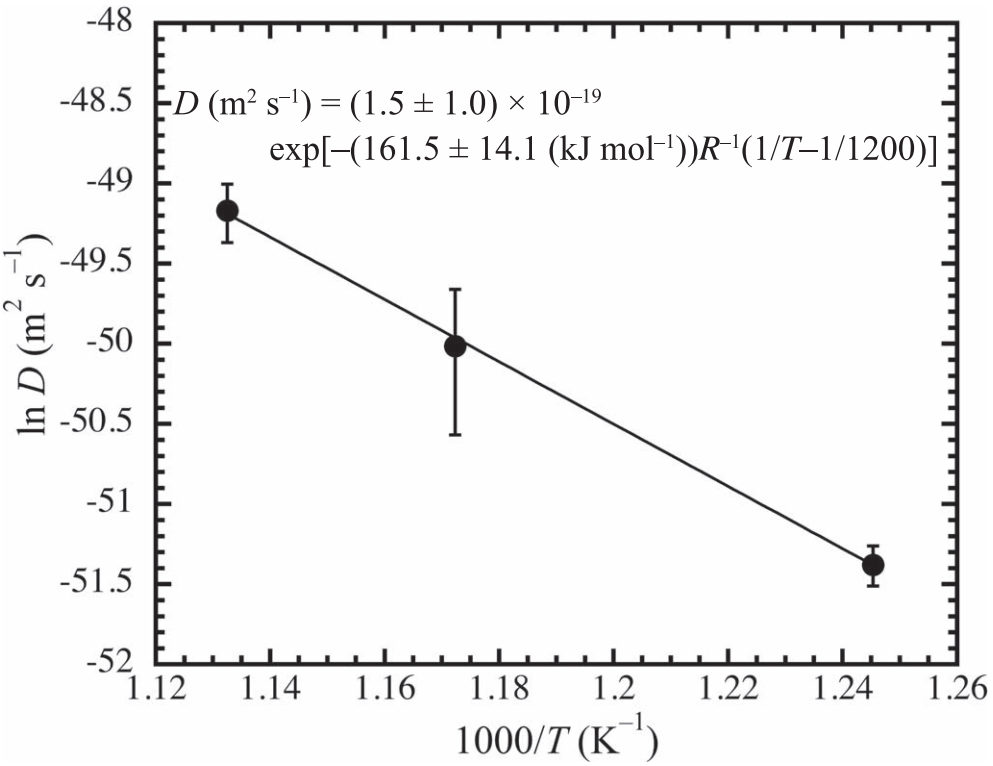

Figure 9. Arrhenius plot of the diffusive isotopic exchange rate constant (D) at P_{H2O} of 0.3 Pa. Errors represent the 1σ standard deviations of the means.

$(1.9 \pm 0.8) \times 10^{-22}$, and $(4.4 \pm 0.8) \times 10^{-22}$ $m^2 s^{-1}$ at 803, 853, and 883 K, respectively. The D shows the Arrhenius relation (Figure 9), yielding D ($m^2 s^{-1}$) $= (1.5 \pm 1.0) \times 10^{-19}$ exp[$-(161.5 \pm 14.1$ (kJ mol^{-1}))$R^{-1}(1/T - 1/1200)$]. The term of $-1/1200$ was included to reduce the uncertainty of the pre-exponential term. This expression of D is valid only below 1200 K, but the extrapolation to >1200 K is meaningless because crystallization of amorphous forsterite proceeds with a minute or less (Yamamoto & Tachibana 2018) at a much faster rate than the oxygen isotopic exchange at 1200 K, as discussed below.

4.1.2. 953, 1073, and 1123 K

Crystallization of amorphous forsterite occurred at 1073 K, and the infrared spectrum is the same as that of isotopically normal crystalline forsterite and shows neither peak shift nor significant peak broadening (Figure 6). The crystallization experiments at 1073 K for the amorphous forsterite preheated at 853 K and 0.3 Pa of $H_2{}^{18}O$ vapor for 120 hr found that the run product shows the infrared spectrum of crystalline forsterite with shifts of all the peak positions to longer wavelengths (Figure 6). Because the amorphous forsterite exposed to $H_2{}^{18}O$ (0.3 Pa) at 853 K for 120 hr should be enriched in ^{18}O as discussed above, the observed shifted peaks represent the infrared feature of ^{18}O-rich crystalline forsterite.

These observations suggest that crystallization occurs faster than oxygen isotopic exchange at 1073 K and that crystalline forsterite does not exchange oxygen isotopes with water vapor as efficiently as amorphous forsterite does. The experiments with crystalline forsterite at 1123 K and 0.3 Pa of $H_2{}^{18}O$ vapor have also shown that crystallization of amorphous forsterite occurs fast and the oxygen isotopic exchange between crystalline forsterite and water vapor is not as fast as that for amorphous forsterite. This is because crystalline forsterite is a nominally anhydrous mineral and does not contain water molecules inside its structure as much as amorphous forsterite does. The slower oxygen isotopic exchange rate with crystalline forsterite is also supported by the oxygen self-diffusion rate in crystalline forsterite (Jaoul et al. 1980).

Crystallization of amorphous forsterite occurred for the samples heated at 953 K and 0.3 Pa of $H_2{}^{18}O$ vapor, and all the peaks of crystalline forsterite shifted to longer wavelengths with time and became broader than those of isotopically normal crystalline forsterite with crystallization (Figure 5). This can be interpreted as indicating that crystallization of amorphous forsterite proceeds after incomplete oxygen isotopic exchange of amorphous forsterite at this temperature. Crystalline forsterite can keep the oxygen isotopic composition at the timing of its crystallization because of the sluggish isotopic exchange reaction, as observed at higher temperatures of 1073 and 1123 K. Thus, forsterite crystallizing in the early stage can be ^{16}O-rich, while that crystallizing in the late stage can be enriched in ^{18}O because the isotopic exchange between amorphous forsterite and $H_2{}^{18}O$ proceeds with time. In this case, the infrared spectrum of the run product should be a mixture of those of crystalline forsterite with a wide range of oxygen isotopic compositions, resulting in the spectrum with broader peaks shifted to longer wavelengths.

It has been known that the change of grain shape and size through sintering during annealing also affects the peak positions and peak widths (e.g., Koike et al. 2010). However, Koike et al. (2010) found that, unlike other peaks of crystalline forsterite, the peak at 11.9 μm is insensitive to the change of grain shape. In the present experiments, we observed that the 11.9 μm peak also shifted to a longer wavelength (Figure 5). Therefore, we conclude that the peak shifts and peak broadening at 953 K were not caused by the changes of grain shape and size but by simultaneous crystallization and oxygen isotopic exchange of amorphous forsterite.

The activation energies of these competing reactions are ~162 kJ mol^{-1} for the diffusive exchange rate constant (Figure 9) and ~357 kJ mol^{-1} for crystallization at P_{H2O} of 0.3 Pa (Yamamoto & Tachibana 2018). Hence, crystallization proceeds at a larger rate at higher temperatures, such as 1073 K, while the isotopic exchange of amorphous forsterite occurs faster at lower temperatures, such as <883 K. The transition temperature for the two competing processes would be close to 953 K.

4.2. Isotopic Exchange Reaction Kinetics at 0.01 Pa of Water Vapor

Temporal changes of the oxygen isotopic compositions of the samples heated at 0.01 Pa of $H_2{}^{18}O$ vapor are summarized in Figure 7. Oxygen isotopic exchange proceeded at smaller reaction rates at 0.01 Pa of $H_2{}^{18}O$ vapor and 883 and 853 K than those at 0.3 Pa of $H_2{}^{18}O$ vapor (Figures 7(b) and (c)). Moreover, the data suggest that the reaction proceeded at almost the same rate at 883 and 853 K at 0.01 Pa of water vapor (Figure 7(a)). These cannot be explained by the diffusive isotopic exchange reaction that controls the overall reaction rate at 0.3 Pa of water vapor and should be controlled by a different process.

A plausible rate-limiting process would be a supply of water molecules to the surface of amorphous particles. The supply flux of water molecules (J_w) depends on P_{H2O} and the mean velocity of water molecules,

$$J_w = \frac{P_{H_2O}}{\sqrt{2\pi mkT}}, \quad (2)$$

where m is a molecular weight of H_2O, k is the Boltzmann constant, and T is the absolute temperature. The J_w does not largely depend on temperature and could explain a very weak temperature dependence of the reaction rate at 883 and 853 K. Moreover, the J_W at 0.01 Pa should be 30 times smaller than that at 0.3 Pa. The supply of water molecules could thus become a rate-limiting process under the lower P_{H2O} conditions.

If this is the case, the temporal change of the degree of isotopic exchange (α) is expressed by

$$\frac{d\alpha}{dt} = \frac{\beta J_w S}{\gamma (V/\Omega) n_A}, \quad (3)$$

where β is a dimensionless parameter to express the isotopic exchange efficiency of colliding water molecules with amorphous forsterite, S is the grain surface area, γ is the atom ratio of oxygen in the gas phase and solid phase (4 for amorphous forsterite and water vapor), V is a volume of the amorphous forsterite grain, Ω is a molar volume of amorphous forsterite, and n_A is Avogadro's number. Equation (3) shows that α changes linearly with time when the supply of water molecules is the rate-limiting process.

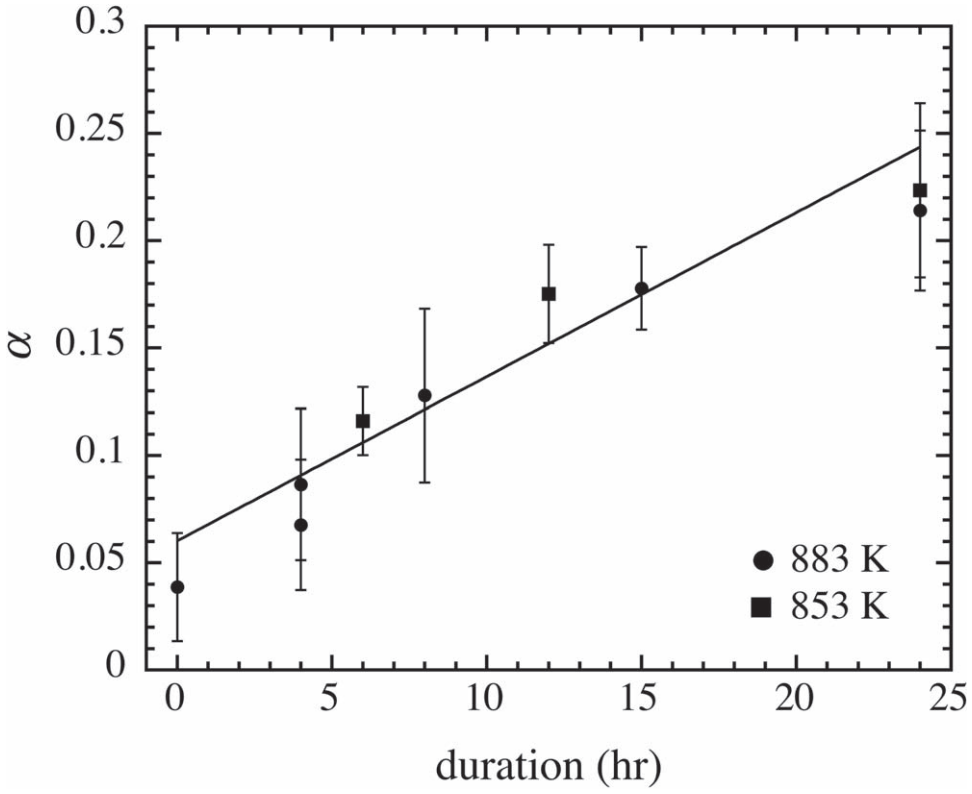

Figure 10. Time evolution of the degree of oxygen isotopic exchange (α) obtained from $\Delta\kappa/\kappa_0$ of samples heated at 883 K (circle) and 853 K (square) and 0.01 Pa of $H_2{}^{18}O$ vapor. The solid line represents the best-fit line by Equation (3). Error bars are the 1σ standard deviations of the means.

The degrees of isotopic exchange (α) of amorphous forsterite heated at 883 and 853 K with 0.01 Pa of $H_2{}^{18}O$ vapor (Figure 10; Table 1) show a linear relation with time. Because the sample that was heated for zero minutes at 883 K showed a small degree of isotopic exchange ($\alpha \sim 0.04$) due to the isotopic exchange upon heating to 883 K, we focus on the slope of the data in Figure 10. The linear regression gives a β of $(7.4 \pm 1.2) \times 10^{-6}$ for the average grain radius of 40 nm.

At 803 K, isotopic exchange proceeded at the identical rate at both 0.01 and 0.3 Pa of $H_2{}^{18}O$ vapor, and the rate at 0.01 Pa of $H_2{}^{18}O$ vapor was slower than those controlled by the supply of water molecules at 883 and 853 K (Figure 7(d)). This suggests that the supply of water molecules is not the rate-limiting step at 803 K and 0.01 Pa of water vapor. The identical reaction rate at 0.01 and 0.3 Pa of $H_2{}^{18}O$ vapor can be explained by the diffusion-controlled isotopic exchange that is expected to have little or no dependence on P_{H2O}.

We thus conclude that the oxygen isotopic exchange rate between amorphous forsterite and water vapor is controlled by the supply of water molecules at lower P_{H2O} and higher temperatures, while it is controlled by the diffusive isotopic exchange reaction within the amorphous structure at higher P_{H2O} and lower temperatures. In the present experimental conditions, the transition of the rate-limiting step occurs at ~850 K and P_{H2O} of 0.01 Pa.

5. Application to Oxygen Isotopic Exchange of Amorphous Forsterite in the Protoplanetary Disks

We evaluated the timescale of oxygen isotopic exchange of amorphous forsterite dust and those of other related reactions in protoplanetary disks. Figure 11 shows the timescales for diffusive oxygen isotopic exchange of amorphous forsterite dust with diameters of 0.08 and 1 μm (solid curves). These grain sizes were chosen for calculation because the average grain size of the starting material is 0.08 μm in this study, and matrix silicate grains in chondrites and presolar silicate grains are typically up to ~1 μm in size (Pontoppidan & Brearley 2010 and references therein; Messenger et al. 2003; Leitner et al. 2012; Hoppe et al. 2015). The timescale of diffusive isotopic exchange is given as r^2/D, which corresponds to the time required for $\alpha \sim 1$. The reaction timescale is shorter than the typical lifetime of gas in protoplanetary disks (1–10 Myr; e.g., Pascucci & Tachibana 2010) at >500 K for 0.08 μm sized grains and >600 K for 1 μm sized grains.

The supply of water molecules from the disk gas can govern the reaction at higher temperatures and lower P_{H2O}. The timescales of oxygen isotopic exchange controlled by the supply of water molecules are also shown in Figure 11 for 0.08 and 1 μm sized amorphous forsterite dust at different P_{H2O} (10^{-1} and 10^{-4} Pa; dotted curves). The P_{H2O} of 10^{-1} and 10^{-4} Pa correspond to the total pressures of 10^2 and 10^{-1} Pa ($H_2O/H_2 \sim 10^{-3}$) of protoplanetary disks, respectively. The reaction timescales were obtained for $\alpha = 1$ (complete isotopic exchange) using Equation (3) with a β of 7.4×10^{-6}. The timescale has a linear dependence on P_{H2O} (Equations (2) and (3)), and it takes three orders of magnitude longer for isotopic exchange at 10^{-4} Pa than at 10^{-1} Pa. Within the possible range of P_{H2O} in protoplanetary disks, the oxygen isotopic exchange timescale of amorphous forsterite would be controlled by the supply of water molecules at >~800 K for P_{H2O} of 10^{-4} Pa and >~1100 K for P_{H2O} of 10^{-1} Pa because the gas flux does not have a large temperature dependence (Equation (2)). We note that β may depend on temperature and might be larger

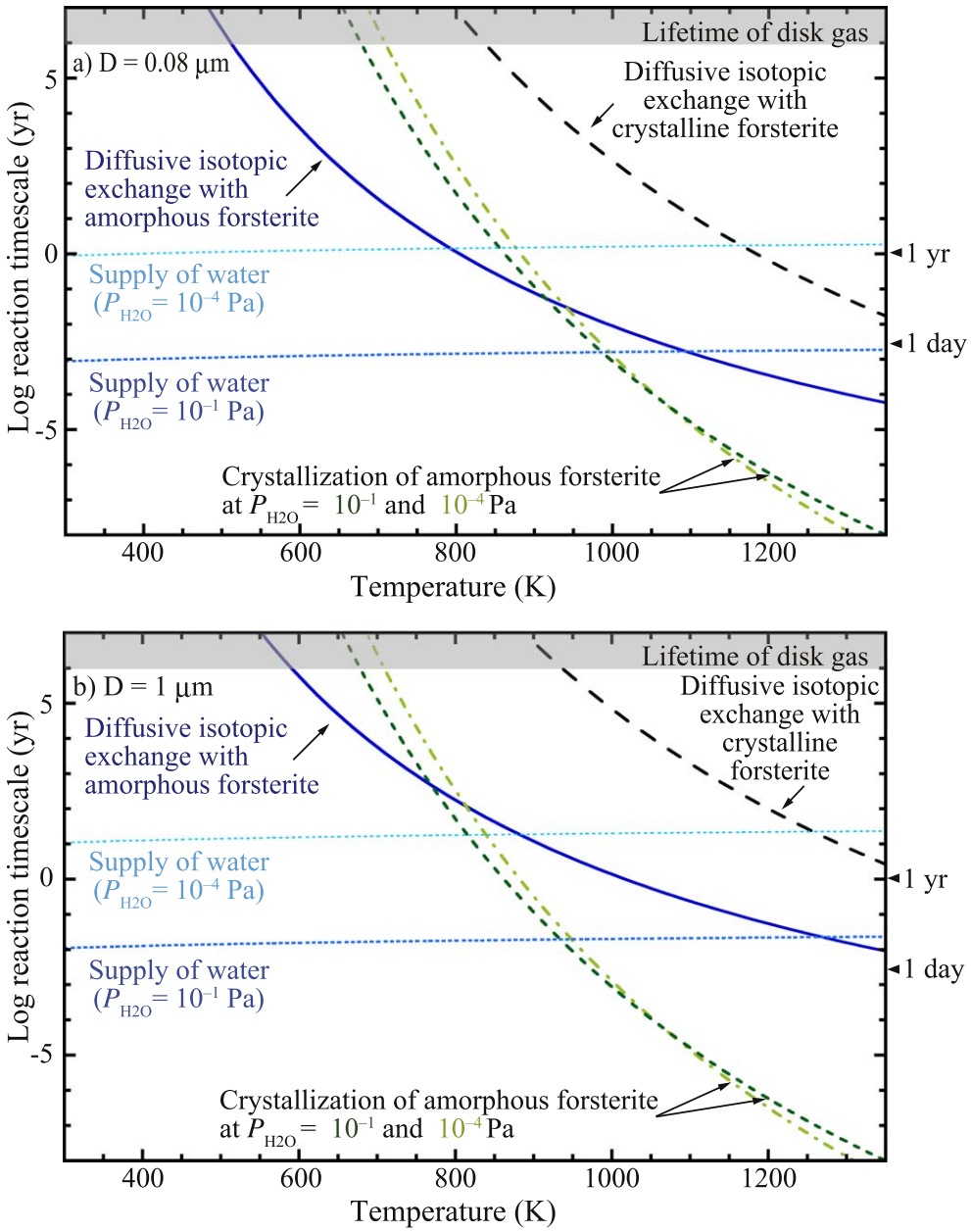

Figure 11. Timescales of oxygen isotopic exchange between amorphous forsterite dust and water vapor in protoplanetary disks controlled by the diffusive isotopic exchange reaction (solid curves) and the supply of water molecules at P_{H2O} of 10^{-1} and 10^{-4} Pa (dotted curves). Timescales of oxygen self-diffusion in crystalline forsterite (long-dashed curves; Jaoul et al. 1980) and crystallization of amorphous forsterite at P_{H2O} of 10^{-1} and 10^{-4} Pa (short-dashed and dotted-dashed curves, respectively; Yamamoto & Tachibana 2018) are shown for comparison. The estimated lifetime of protoplanetary disk gas (1–10 Myr) is also shown for comparison. (a) 0.08 μm. (b) 1 μm.

at higher temperatures. If this were the case, the reaction timescale would become shorter at higher temperatures.

Crystallization of amorphous forsterite due to thermal annealing is also considered. The timescale of crystallization of 0.08 μm sized amorphous forsterite grains (Yamamoto & Tachibana 2018) at a P_{H2O} of 10^{-1} and 10^{-4} Pa are also shown in Figure 11 (short-dashed and dotted-dashed curves, respectively). The crystallization timescale for 1 μm sized amorphous forsterite would not be largely different from that shown in Figure 11 according to the kinetics reported in Yamamoto & Tachibana (2018), where crystallization occurs from preexisting nuclei in the grains. Because the activation energy for crystallization of amorphous forsterite (254–414 kJ mol^{-1} for a P_{H2O} of 10^{-4}–500 Pa) is larger than that for the diffusive isotopic exchange reaction, amorphous forsterite can crystallize prior to the oxygen isotopic exchange if the grains are rapidly heated at temperatures above 800–900 K, as observed in this study.

The oxygen isotopic exchange between crystalline forsterite and water vapor would be controlled by the supply of water molecules or self-diffusion of oxygen within the crystalline structure. The timescales of oxygen self-diffusion in 0.08 and 1 μm sized crystalline forsterite grains (Jaoul et al. 1980) are also shown in Figure 11 (long-dashed curves). The β for the water supply–controlled isotopic exchange for crystalline forsterite is not known but may not be significantly smaller than that for amorphous forsterite. If the same β can be used, the timescales of isotopic exchange for crystalline forsterite

controlled by the supply of water molecules are the same as those for amorphous forsterite (dotted curves in Figure 11), and the oxygen isotopic exchange should occur by oxygen self-diffusion within crystalline forsterite. The diffusive isotopic exchange between crystalline forsterite and water vapor is significantly slower than that for amorphous forsterite. The timescale for isotopic exchange of crystalline forsterite would be ~4–5 orders of magnitude longer than that for amorphous forsterite (Figure 11), and the effective isotopic exchange would not occur with short-duration heating at ~1000 K. In this case, the original isotopic signature of amorphous forsterite dust would be kept in crystalline forsterite dust transformed from amorphous forsterite.

To summarize, amorphous forsterite dust with a diameter of $<1\ \mu$m could exchange oxygen isotopes within the disk lifetime if it was heated at temperatures higher than ~500–600 K, and the dust should have been kept at <500 K to preserve its original isotopic signature.

Silicate grains from comet 81P/Wild 2 had ^{16}O-poor isotopic compositions close to the terrestrial composition (McKeegan et al. 2006; Nakamura et al. 2008). If primordial silicate dust in the solar system was ^{16}O-rich, the ^{16}O-poor isotopic signatures of silicate dust in cometary materials implies that cometary silicate dust would be processed at temperatures higher than 500–600 K prior to their accretion into the comet by heating processes such as thermal annealing in the inner solar system, followed by large-scale radial transport. The oxygen isotopic signatures of presolar amorphous silicate grains would also be easily erased by heating at >500 K.

6. Conclusions

The kinetics of the oxygen isotopic exchange reaction between amorphous forsterite and water vapor under protoplanetary disk-like low-pressure conditions was experimentally investigated. The amorphous forsterite samples were heated at 803–1073 K for 0–336 hr at 0.3 or 0.01 Pa of $H_2{}^{18}O$ (or $H_2{}^{16}O$) vapor. The heated samples were examined with infrared spectroscopy, X-ray diffraction, and SIMS to determine the existing phases and the degree of oxygen isotopic exchange.

Amorphous forsterite exchanged its oxygen isotopes with water vapor while keeping the amorphous structure at 803–883 K. Temporal changes of the degree of isotopic exchange of amorphous forsterite at water vapor pressure (P_{H2O}) of 0.3 Pa were governed by a diffusive isotopic exchange reaction in the amorphous structure, yielding the isotopic exchange rate $D\ (m^2\ s^{-1}) = (1.5 \pm 1.0) \times 10^{-19}$ exp $[-(161.5 \pm 14.1\ (kJ\ mol^{-1}))R^{-1}(1/T - 1/1200)]$. Both crystallization and oxygen isotopic exchange of amorphous forsterite proceeded in parallel at 953 K and P_{H2O} of 0.3 Pa. Crystallization of amorphous forsterite dominated over oxygen isotopic exchange at 1073 K and a P_{H2O} of 0.3 Pa, and no oxygen isotopic exchange was observed. This is because the crystallization rate is larger than the isotopic exchange rate at higher temperatures and the isotopic exchange between crystalline forsterite and water vapor is more sluggish than that for amorphous forsterite.

At a P_{H2O} of 0.01 Pa, the isotopic exchange at 853 and 883 K proceeded at the almost identical rate, which can be explained by the reaction controlled by the supply of water molecules. On the other hand, the reaction at 803 K and a P_{H2O} of 0.01 Pa was controlled by the diffusive exchange reaction as at a P_{H2O} of 0.3 Pa because the diffusive exchange reaction becomes slower than the supply of water molecules at lower temperatures due to its larger temperature dependence.

Under T–P_{H2O} conditions in protoplanetary disks, the diffusive oxygen isotopic exchange reaction could be responsible for the oxygen isotopic evolution of submicron-sized amorphous forsterite dust below ~900 and ~800 K at water vapor pressures of 10^{-1} and 10^{-4} Pa, respectively. The supply of water molecules from the vapor phase could control the oxygen isotopic exchange reaction at higher temperatures. However, when amorphous forsterite crystallized rapidly at such high temperatures, the oxygen isotopic exchange would be controlled by oxygen self-diffusion in crystalline forsterite, and the required timescale for oxygen isotopic exchange would become significantly longer than that for amorphous forsterite.

The diffusive isotopic exchange rate indicates that the oxygen isotopic exchange reaction between ^{16}O-rich amorphous forsterite dust and ^{16}O-poor water vapor could proceed within a lifetime of protoplanetary disk gas (1–10 Myr) at temperatures above 500–600 K, and that the oxygen isotopic signatures of primordial and/or presolar amorphous forsterite dust could be preserved only if the dust was kept at temperatures below 500–600 K in the early solar system.

We acknowledge Akira Tsuchiyama for providing the amorphous forsterite powder and an anonymous reviewer for constructive comments. This work was financially supported by a Grant-in-Aid for JSPS Research Fellow (17J05044) and Ministry of Education, Sports, Science and Technology KAKENHI grant.

ORCID iDs

Daiki Yamamoto https://orcid.org/0000-0001-6852-2954
Shogo Tachibana https://orcid.org/0000-0002-4603-9440

References

Abe, K., Sakamoto, N., Krot, A. N., & Yurimoto, H. 2017, GeocJ, 51, 3
Crank, J. 1975, The Mathematics of Diffusion (2nd ed.; Oxford: Oxford Univ. Press)
Doremus, R. H. 1969, in Reactivity of Solids, ed. J. W. Mitchell et al. (New York: Wiley), 667
Floss, C., & Haenecour, P. 2016, GeocJ, 50, 3
Floss, C., & Stadermann, F. J. 2012, M&PS, 47, 992
Hoppe, P., Leitner, J., & Kodolányi, J. 2015, ApJ, 808, L9
Jaoul, O., Froidevaux, C., Durham, W. B., & Michaut, M. 1980, E&PSL, 47, 391
Kemper, F., Vriend, W. J., & Tielens, A. G. G. M. 2004, ApJ, 609, 826
Koike, C., Imai, Y., Chihara, H., et al. 2010, ApJ, 709, 983
Kuroda, M., Tachibana, S., Sakamoto, N., et al. 2018, AmMin, 103, 412
Leitner, J., Vollmer, C., Hoppe, P., & Zipfel, J. 2012, ApJ, 745, 38
McKeegan, K. D., Aléon, J., Bradley, J., et al. 2006, Sci, 314, 1724
McKeegan, K. D., Kallio, A. P. A., Heber, V. S., et al. 2011, Sci, 332, 1528
Messenger, S., Keller, L. P., Stadermann, F. J., et al. 2003, Sci, 300, 105
Nakamura, T., Noguchi, T., Tsuchiyama, A., et al. 2008, Sci, 321, 1664
Nguyen, A. N., Berger, E. L., Nakamura-Messenger, K., et al. 2017, M&PS, 52, 2004
Pascucci, I., & Tachibana, S. 2010, in Protoplanetary Dust: Astrophysical and Cosmochemical Perspectives, ed. D. Apai & D. S. Lauretta (New York: Cambridge Univ. Press), 263

Pontoppidan, K. M., & Brearley, A. J. 2010, in Protoplanetary Dust: Astrophysical and Cosmochemical Perspectives, ed. D. Apai & D. S. Lauretta (New York: Cambridge Univ. Press), 191
Ratzka, T., Leinert, C., Henning, T., et al. 2007, A&A, 471, 173
Sakamoto, N., Seto, Y., Itoh, S., et al. 2007, Sci, 317, 231
Seto, Y., Sakamoto, N., Fujino, K., et al. 2008, GeCoA, 72, 2723
Tachibana, S., Nagahara, H., Ozawa, K., et al. 2011, ApJ, 736, 16
van Boekel, R., Min, M., Waters, L. B. F. M., et al. 2005, A&A, 437, 189
Yamamoto, D., & Tachibana, S. 2018, ESC, 2, 778
Yurimoto, H., & Kuramoto, K. 2004, Sci, 305, 1763